Considerations on data acquisition in laser ablation – ICP-mass spectrometry with low-dispersion interfaces

Stijn J. M. Van Malderen[a], Johannes T. van Elteren[b], Vid S. Šelih[b], and Frank Vanhaecke[a,*]

[a]*Department of Analytical Chemistry, Ghent University, Campus Sterre, Krijgslaan 281 - S12, B-9000 Ghent, Belgium*

[b]*Department of Analytical Chemistry, National Institute of Chemistry, Hajdrihova 19, SI-1000 Ljubljana, Slovenia*

[*]*Corresponding author. E-mail address: Frank.Vanhaecke@UGent.be, fax number: +32 9 264 4960*

1. Abstract

This work describes the temporal skew effects induced by undersampling the high-frequency signal patterns generated by a laser ablation-inductively coupled plasma-mass spectrometer equipped with a low-dispersion ablation cell and sequential mass analyzer. By characterizing the width of the signal peak generated from a single shot on the sample, critical experimental parameters, such as the laser repetition rate and detector cycle timings for the individual nuclides can be matched so as to avoid these imaging artifacts (aliasing) induced by an insufficient sampling rate. By increasing the laser repetition rate by a factor 2-3, masses at the end of the mass scan can be sampled at higher sensitivity. Furthermore, the dwell times can be redistributed over the nuclides of interest based on the signal-to-noise ratio to increase the image contrast.

Keywords: 'LA-ICP-MS', 'spectral skew', 'acquisition', 'artifacts', 'contrast'

2. Introduction

Mass analyzers which scan over the mass range – *e.g.*, a quadrupole mass analyzer that at any given time only transmits ions within a narrow bandpass window (typically ~0.5 amu) to the detector, or a double-focusing sector field mass spectrometer of Nier-Johnson geometry that at any given time focuses only the ion beam for ions within a defined mass-to-charge ratio range onto the detector – are the most widely deployed type in ICP-mass spectrometry (ICP-MS). This type of single-collector sequential scanning mass spectrometer may however not be very suitable for detecting fast transient signals, as encountered in laser ablation (LA)–ICP–MS or single-particle ICP-MS.[1] As the mass analyzer can only detect ions within a narrow m/q range at any given moment, real-time information on the transient signal shape at another m/q is lost, and spectral skew and aliasing are introduced as a result of the relatively low sampling rate, as previously described in literature.[2] Quasi-simultaneous mass spectrometers equipped with detectors with low signal rise times, *e.g.*, time-of-flight mass spectrometers, suffer much less from these sampling artefacts.[3] Most currently available LA-systems are capable of producing a signal peak for a single laser shot with a full width at 1% of the maximum of < 200 ms.[4, 5] This means that the response for single shots at frequencies $\leq 5\,Hz$ can be resolved. Thus, a response for each individual pixel (laser shot) in a LA-ICP-MS map can be acquired separately, resulting in spatially resolved pixels.[6] In conventional continuous mode mapping (line scanning), the repetition rate of the laser is increased or a smoothing device is used to achieve a stable response, by overlapping of the fast subsequent signals, thus blurring the signal peaks.[7-10] For a homogeneous sample, a stable signal (for every m/q) can be sampled at any given moment, and will result in a stable number of integrated counts in each acquisition block, and thus, a stable count rate. Low-dispersion aerosol transport systems, first introduced in 2013, permit single-shot signal peaks with a full width at 1% of the maximum of < 10 ms, thus, frequencies of 0.3 – 1 kHz are required to smooth the signal.[4, 5] Increasing the repetition rate to >0.3-1 kHz is however undesirably: i) the laser will sample more material, over an extended depth, worsening depth resolution and elemental fractionation[11], ii) the response from many sampling positions will be mixed in a single larger pixel value, deteriorating the resolution to more than twice the spot size[12, 13], iii) for ns-lasers, the increased frequency will lead to a higher laser gas consumption and reduce the lifetime of the laser components (e.g., flash lamp, high-voltage circuit), resulting in costly repairs. It should also be noted that not all lasers can operate at repetition rates >0.1 kHz. Femto-second lasers are more capable in this aspect.[14] This work aims to describe, in detail, the nature and origin of the aliasing artefacts in the response as a result of undersampling or oversampling the transient signal with sequential mass spectrometers. Furthermore, a strategy is outlined to overcome these temporal aliasing effects, and achieve an optimal balance between the sampling frequency, data acquisition settings, spot size, and lateral scan speed to create images with laterally resolved pixels of high contrast for every nuclide, and the best possible lateral resolution, at the highest possible throughput rate.

3. Materials and methods

3.1. Samples

NIST (National Institute for Standards and Technology, Gaithersburg, MD, USA) standard reference material 612 (Trace elements in glass), a well-characterized silicate glass standard, was used as a target for all experiments.[15] Three nuclides, with different characteristics in terms of mass number, and level of spectral interference were selected in order to demonstrate the validity of the approach under various conditions.[16] ^{57}Fe, a spectrally interfered (^{40}Ar^{16}O^{1}H^{+}, ^{40}Ca^{16}O^{1}H^{+}, ^{40}Ar^{17}O^{+} and ^{38}Ar^{18}O^{1}H^{+}), minor (2.1%) isotope of Fe (51±2 µg/g), was selected as a low-mid mass range element with challenging spectral interference properties.[17] ^{115}In (In concentration: 38.9±2.1 µg/g, isotopic abundance: 95.7%) was chosen as a mid-mass range element with a low level of spectral interference (if any). ^{238}U (U concentration: 37.4±0.1 µg/g, isotopic abundance: 99.3%) was chosen as a high-mass element with a very low level of spectral interference (if any). The variety presented by these 3 nuclides should cover many situations. In the center region of NIST SRM 612, these elements are distributed homogeneously on a microscopic scale; the variation observed in NIST SRM 610, a very similar reference material has been shown to be ≤ 1% by Hinton *et al.* on a 10 μm scale.[18, 19]

3.2. Instrumentation

All experiments were performed using an Analyte G2 193 nm ArF* excimer-based laser ablation (LA) system (Teledyne Photon Machines, Bozeman, MT, USA), coupled to a quadrupole-based Agilent 7900 ICP-MS instrument (Agilent, Tokyo, Japan). The LA-system was equipped with a HelEx II 2-volume ablation cell. Helium was used as a carrier gas for aerosol transport from the sample surface to the ICP and was mixed downstream with Ar as a make-up gas flow in an ARIS (Aerosol Rapid Introduction System) mixing bulb before entering the plasma.[20] The ARIS was developed at Ghent University and is meanwhile commercially available from Teledyne Photon Machines. Operational parameters of the ICP-MS instrument and LA-unit were tuned for maximum sensitivity (for ^{7}Li, ^{115}In, and ^{238}U), low oxide formation based on the ^{238}U^{16}O^{+}/^{238}U^{+} ratio and low laser-induced elemental fractionation based on the ^{238}U^{+}/^{232}Th^{+} ratio using NIST SRM 612. The optimal conditions were achieved at a radiofrequency (RF) power of 1550 W and cool gas (Ar), auxiliary gas (Ar) and make up gas (Ar) flow rates of 13, 0.70 and 0.68 L min^{-1}, respectively. The carrier gas (He) flow rate was optimized to 0.58 L min^{-1}.

3.3. Signal aliasing experiments

In order to study the systematic aliasing effects, previously observed in a number of studies[2, 21-25], various scans were undertaken on NIST SRM 612 using multiple data acquisition settings, which are critically important to the occurrence of these sampling artifacts. In a first instance, the laser was run at a low repetition rate, for each nuclide of interest individually, at a high sampling (or data acquisition) rate (f_s), *i.e.* a short detector sampling cycle time (f_s^{-1}). The most relevant LA and detector

acquisition settings used in this first part of the experiment are described in Table 1.

Table 1 Lasing and detector parameters for individual (single-m/q) runs

Energy density [$J\ cm^{-2}$]	3.5
Repetition rate [Hz]	5
Scan mode	Fixed repetition rate, speed
Scan length [mm]	2
Scan speed [$\mu m\ s^{-1}$]	100
Number of shots per position	1
Beam waist diameter [μm]	20
Mask shape	Square
Acquired m/q	57 ($^{57}Fe^{+}$)
(separate single-m/q runs)	115 ($^{115}In^{+}$)
	238 ($^{238}U^{+}$)
Sampling cycle [ms]	3
Dwell time per m/q [ms]	3

This part of the experiment allowed to characterize the washout of each nuclide. Note that the dispersion characteristics can be nuclide-dependent, and vary with the distribution of the nuclide across the aerosol phases. Particulates with a narrow particle size distribution may be transported as dense aerosol clusters, as a result of their similar drag coefficients and small mean free path lengths, whilst gaseous phases may suffer from increased diffusion of the aerosol cloud as a result of the larger mean free path.[26] Once the washout characteristics of the nuclides are known, the acquisition cycle timing can be optimized. When a relatively slow detector samples a high-frequency signal, aliasing may occur. This type of temporal aliasing effect in the transient signal is not to be confounded with spatial aliasing as a result of undersampling an object in the image.[13] In this study, spectral skew and aliasing effects were deliberately generated in the second part of the experiment by varying the detector acquisition cycle times. The corresponding experimental parameters are described in Table 2.

Table 2 Lasing and detector parameters for undersampling/oversampling – all other settings are kept as in Table 1.

Repetition rate [Hz]	80
Scan length [mm]	2.4
Scan speed [$\mu m\ s^{-1}$]	800
Number of shots per position	1
Beam waist diameter [μm]	20
Acquired m/q (within the same multi-element runs)	57 ($^{57}Fe^{+}$), 115 ($^{115}In^{+}$) and 238 ($^{238}U^{+}$)
Minor undersampling detector settings	
Sampling cycle [ms]	25.103
Dwell time [ms]	4.7, 4.7 and 4.7, respectively
Minor oversampling detector settings	
Sampling cycle [ms]	24.903
Dwell time [ms]	4.7, 4.7 and 4.5, respectively
Major undersampling detector settings	
Sampling cycle [ms]	70.003
Dwell time [ms]	20.0, 19.0 and 20.0, respectively
Major oversampling detector settings	
Sampling cycle [ms]	20.002
Dwell time [ms]	3.0, 3.0 and 3.0, respectively
In-sync detector settings	
Sampling cycle [ms]	25.003
Dwell time [ms]	4.7, 4.7, and 4.6, respectively

In Table 3, the optimized set of detector acquisition cycle settings used in the third part of this experiment are provided. These settings were calculated using the strategy outlined in the next section.

Table 3 Optimized detector timings

Dwell time for ^{57}Fe [ms]	13.8
Dwell time for ^{115}In [ms]	0.1
Dwell time for ^{238}U [ms]	0.1
Sampling cycle [ms]	25

3.4. Effect of undersampling on multi-nuclide bioimaging experiments

The importance of the considerations highlighted in this work is demonstrated in a bioimaging experiment on liver tissue sections, in which P, Mn, and K were mapped. The sections were cut to a thickness of 15 µm as described by Costas-Rodriguez *et al.*[27]. Table 4 describes the LA-ICP-MS settings for mapping.

Table 4 Lasing and detector parameters for the bioimaging experiment.

Repetition rate [Hz]	40
Scan length [mm]	1000
Scan speed [$\mu m\ s^{-1}$]	100
Number of shots per position	2
Beam waist diameter [μm]	5
Acquired m/q (within the same multi-element runs)	31 ($^{31}P^{+}$), 39 ($^{39}K^{+}$), and 55 ($^{55}Mn^{+}$)
FW0.01M	50.9 ($^{31}P^{+}$), 41.2 ($^{39}K^{+}$), and 48.9 ($^{55}Mn^{+}$),

4. Results and discussion

4.1. Peak width and pixel acquisition rate

The full peak width at 1% of the maximum intensity (FW0.01M) is an important characteristic of the dispersion (Table 4), as it describes how much time it takes for the response to drop down two orders of magnitude, *i.e.* it describes how fast pixels can be acquired whilst ensuring that differences in the response of up to two orders of magnitude in neighboring pixels can be distinguished. The threshold for the importance of this bleed-over effect is application-dependent. For the setup used in this study, the peak profile FW0.01M of the nuclides of interest are all below 25 ms (Table 5).

Table 5 Statistics on the washout of the three nuclides under investigation

Nuclide	RSD Area [%]	FWHM [ms]	FW0.01M [ms]
^{57}Fe	9	14±1	23±1
^{115}In	8	8±1	21±1
^{238}U	13	9±1	20±1

The maximum laser repetition rate f_{max} and pixel acquisition rate R_A (assuming a single shot per ablation position) at which the response is temporally, and thus also spatially, resolved, is equal to $R_A = f_{max} = 1/FW0.01M$. In this case, a temporally and spatially resolved response can be maintained up to an R_A of $40Hz$ ($f = 40Hz$). As such, the translation speed can thus be determined as $v = R_{spot} \times R_A$, with R_{spot} the width of the laser spot in the scanning direction.

4.2. Spectral Skew/aliasing

Sampling this 'pulse-resolved' transient signal may introduce under- and oversampling (upsampling) effects. By oversampling

the signal, *i.e.* by sampling the transient signal at a rate much higher than the laser ablation frequency, the peak shape of the response for every single laser shot can be described in detail; adequate integration of the single peaks in post-processing requires each peak to be sampled >7-10 times (Figure 1); any less, the peaks become non-resolved, and the accuracy of the peak area integration for each individual peak is severely deteriorated with a bias >10% (Figure 1) as it becomes increasingly difficult to attribute a single data point to a single peak.

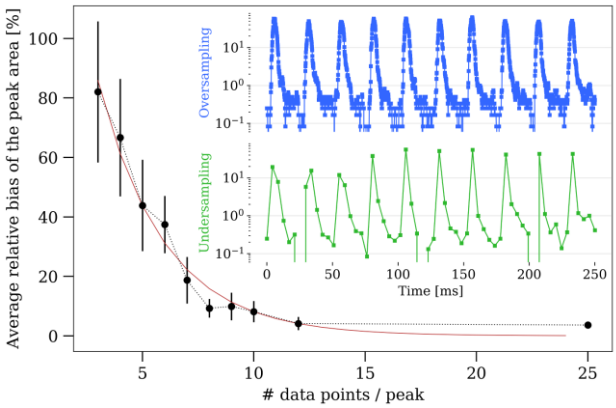

Figure 1 Graph of the relationship between the number of data points sampled per peak and the relative bias introduced within the peak area. This graph was constructed by artificially decreasing the sampling rate of an oversampled transient signal of baseline-separated peaks (^{238}U; repetition rate 40Hz), shown in the figure inset. The error bars are 2s uncertainty on the average bias.

The relative standard deviation on the peak area of a set of 1000 peaks is ~5 %, hence, an average bias in the integration of the peak area of 5-10 % would be acceptable for most imaging applications. The cut-off frequency for integrating individual peaks is thus $\gtrsim 10 f_{max}$. Fast sampling of the signal, *e.g.*, at >100Hz (or a dwell time < 10 ms), however, results with most ICP-MS units in a dramatic decrease of the duty cycle, as the fraction of the time devoted to mass analyzer transition and settling is increasing with respect to the actual (dwell) time devoted to signal acquisition. For example, a settling time of 3 ms for a mass scan containing 2 m/q will result in a duty cycle of <40 % at a sampling frequency of 100 Hz. When, on the other hand, the detector sampling rate f_s lies below the Nyquist frequency $(2f)$, the responses captured by each acquisition block (within the corresponding dwell time) reflect the counts from f/f_s peak profiles. When $f/f_s \notin \mathbb{N}$ (or in other words, is not a positive integer number >0), the position of the acquisition block will shift in time relative to the peak profile position, resulting in a change of the response or signal intensity, as demonstrated in Figure 2.

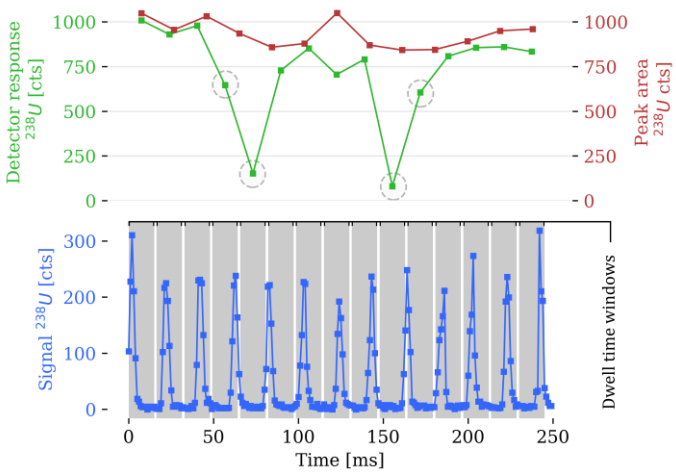

Figure 2 Representation of the detector sampling desynchronization process resulting in the distortion of the signal into a waveform which does not reflect the stable peak area. Data points outside of the expected range are circled. Repetition rate set to 50 Hz. The mass filter floats onto a single m/q, but the detector is blind to incoming ions after each acquisition block due to a short delay introduced by resetting the digitizer.

This *desynchronization* process is periodic, resulting in a low-frequency wave pattern (Moiré pattern) in the detector response or signal intensity within the scan, despite the stable peak areas. It is important to realize that the wave pattern reflects the change in the position of the acquisition window relative to the peak profile, and not the actual response for the nuclide. When the laser repetition rate and the sampling rate are almost synchronized, the signal may show a soft gradient, which can be easily misinterpreted as an endogenous concentration gradient (Figure 3B-C). More information on this topic is present in the supplementary information. Spectral skew, i.e. the spatio-temporal shift between the different mass channels, is also clearly present as a phase shift in the response (this is clearly seen in Fig. 3B).

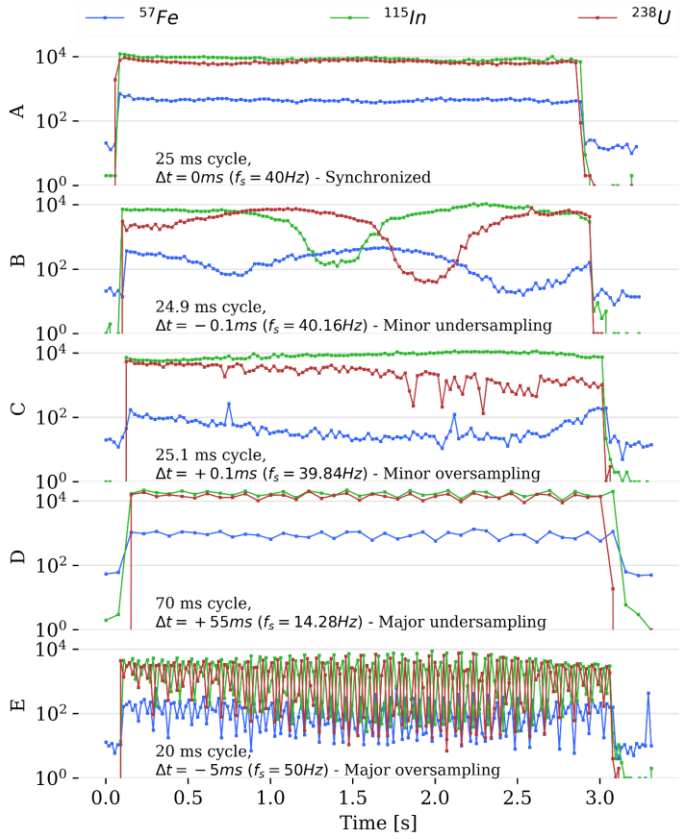

Figure 3 Raw detector response from scanning NIST SRM 612 using various detector timings, demonstrating the difficulties in matching repetition rate and acquisition settings. All experiments conducted with a repetition rate of 80 Hz (Table 2).

4.3. Avoiding aliasing

To circumvent the occurrence of wave patterns, the laser repetition rate (or one of its harmonics) and the sampling cycle frequency need to be matched ($f = N \cdot f_s$, with $N \in \mathbb{N}$) as this results in the integration of an integer number of peaks within a single acquisition block – translating the response into a single pixel value. When using this approach, mapping can be performed at high throughput, as the ion flux does not need to be stabilized to obtain a stable sensitivity. Anti-aliasing reconstruction approaches are not an attractive alternative here due to the high level of shot noise. For multi-nuclide scans however, another issue appears when $f = f_s$: for the m/q values scanned in the last part of the detector cycle, the signal intensity is probed on the slope of the (non-symmetrical) single-pulse response peak, thus resulting in a low sensitivity for these nuclides (Figure 4, red signal at 40 Hz).

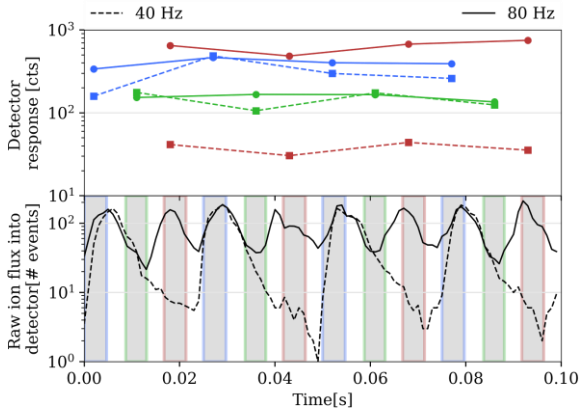

Figure 4 Graph demonstrating the effect of doubling the laser repetition rate with a synchronized detector, for a multi-nuclide scan. The response in the upper part was modeled based on an experimental ion flux as detected on the $^{238}U^+$ channel.

To address this problem, the laser repetition frequency can be doubled or tripled to achieve sampling near the maximum intensity for every nuclide, whilst maintaining a stable response (Figure 4). In this case, each single sampling cycle captures the signals generated in 2 subsequent laser shots ($f = 2f_s = 80\ Hz$), which cannot be distinguished spatially or temporally (the pixel acquisition rate R_A remains the same as before: $R_A = f_s = 1/FW0.01M$). When N>1, there will invariably be non-negligible contribution of previous laser shots (which are at a different ablation position) to the value of the pixel representing the current shot effect as a result of signal carryover; this memory effect aggravates when N increases and will affect the lateral resolution and contrast ratio of 2 neighboring pixels in the scan direction. This is why N=2 is preferred over N=3 as a compromise situation. Even when the aliasing effects are modulated by synchronizing the laser repetition rate and the sampling cycle frequency, spectral skew will still be present for sequential mass analyzers. As a result, for continuous-mode line-based mapping approaches, the response for every line will be shifted in phase (and sensitivity) due to a delay introduced by the time required for the translation stage to travel to the start of each line and the time required by the laser ablation system to start firing the laser. When the laser system triggers the ICP-MS over TTL to start a new recording for every line, this problem persists, due to the inconsistent timing (jitter) of the laser trigger mechanism and the ICP-MS software-based solution for initiating a new recording. Increasing the laser repetition rate only partly mitigates this problem.

4.4. Improving the image contrast

Though the strategy outlaid in the previous section allows for a stable signal to be obtained, Poisson-type detector noise, which dominates the background at low count rates, is still the limiting factor in the detection of the spatial distribution of the nuclides in the absence of spectral interferences. In order to optimize the image contrast for all n nuclides simultaneously, the following workflow is adopted: i) a single scan is performed across the image, using a spot size large enough for the response or signal intensity for each nuclide to be well above the background level (>1 order of magnitude higher), to determine the signal-to-noise ratio (SNR); ii) the dwell times for each nuclide N_i is determined based on the SNR. This means that the total available dwell time within each acquisition cycle is distributed across the nuclides $t_{dwell,tot} = \sum_n^1 t_{dwell,N_i}$; iii) the spot size is optimized to achieve the best

possible lateral resolution for an acceptable image contrast. A Bayesian signal detection theory (SDT) adaptation of the Rose model is employed as a decision criterion. As a measure of image fidelity of ergodic systems (the element distribution being imaged is presumed to be stable during the course of the analysis), an SDT-definition of the Rose-defined SNR which takes into account the shot noise and the size of the object, $SNR_{N_i} = (\mathrm{N}^{0.5}|\langle I_{\mathrm{N_i}}\rangle - \langle \mathrm{I_b}\rangle|)/s_n$ was preferred here over a measure of contrast, *e.g.*, the Weber or modulation contrast, as it more directly reflects the ability of the system to discern objects from the noise.[28, 29] $\langle I_b\rangle$ is here the time-averaged response for the sample substrate, and s_n the standard deviation on the image noise for a single pixel, which includes the heterogeneity in the substrate, and the noise of the detection system. N is the number of pixels in the feature to be identified, which can be predicted based on the dimensions of the features to be sampled and the spot size or scan interspacing. The Rose model is only valid in the limit of low-contrast signals, *i.e.* when the Poisson noise distribution approaches the Gaussian distribution. Hence, to fall within the range of validity of the model, the pre-imaging scan intensity must be well above background. SNR is however not an ideal metric for image quality evaluation as it is only valid for a statistically uncorrelated distribution of image quanta. It does not describe well the noise texture. Alternatively, the detective quantum efficiency (DQE), a measure for image quality in digital X-ray imaging devices, can be used to evaluate image quality (supplementary information).

After the pre-imaging scan, the SNR is calculated for all m/q values monitored. The total available dwell time is redistributed based on the SNRs; the optimal dwell time for nuclide N_i can be estimated as:

$$t_{dwell,N_i} = \frac{\left(\sum_n^1 SNR_{N_i}\right)}{SNR_{N_i}} \frac{t_{dwell,tot}}{\sum_n^1 \left(\frac{\sum_n^1 SNR_{N_i})}{SNR_{N_i}}\right)} \quad (1)$$

As such, the nuclides characterized by a low signal intensity and/or high noise levels, are attributed a longer dwell time relative to other nuclides (Table 3, Figure 5). This equalizes the SNR of all nuclides.

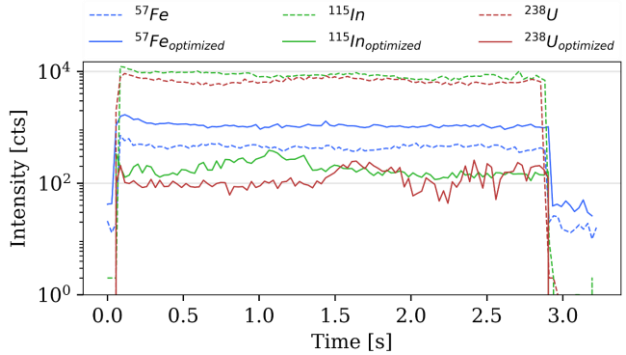

Figure 5 Comparison of the signal intensities obtained using uniformly distributed dwell times and the optimally distributed dwell times, respectively.

Determination of the standard deviation of the image noise may not be straightforward: the detector noise, the noise in the gas background, the (stochastic) shot noise, all underestimate the overall noise level in the image. The variation in the signal only partially reflects the overall noise level, as it also reflects the underlying variability of the (biological) sample. Owing to the destructive nature of LA-ICP-MS, it is also difficult to extract the s_n from two consecutive images on the same area. In order to estimate the s_n from the pre-imaging scan, the underlying variation of the object could be modelled using a spline function. The residual high-frequency variation is then thought to be the noise in the image. More research is needed to determine the best method to estimate the image noise in LA-ICP-MS. It can be noted that LA-ICP-MS noise can be considered to be correlated across multiple pixels in some instances, as carry-over and memory effects may introduce prolonged washout effects over a number of neighboring pixels next to hot spots.

As an initial approximation of the threshold SNR, k, the Rose Criterion indicates that the minimum acceptable contrast requires a $SNR \geq 3-7$, though, a $SNR \geq 4.9$ is preferred.[29] As a result, the spot size can be lowered to a point where SNR = 4.9. In post-processing, the display contrast can be improved further by changing the response function, at the cost of a loss of linearity, which is often undesirable. The minimal (sensitivity-limited) spot radius for a $SNR = k$ can be predicted:

$$R_{min} = R_{cur}\left(\frac{ks_n + \langle I_b\rangle}{SNR_{cur}s_n + \langle I_b\rangle}\right)^{1/n} \quad (2)$$

with R_{cur} the current spot radius and SNR_{cur} the current SNR ((2 is only valid for circular spots). For spot radii > 2 µm, $n \approx 2$, whilst for spot radii < 2 µm, $n \approx 3$, as not only the surface area, but also the ablation efficiency decreases due to Gaussian beam shape formed as a result of diffraction effects. Depending on the sample, it is not always the best practice to work at the sensitivity-limited spot radius, as the Nyquist rate, the sample area, the desired accuracy of the results, and the overall sample throughput should also be taken into account. Once a spot size is set, the stage translation speed v can be recalculated using $v = R_{spot} \times R_A$.

4.5. Effect of aliasing on multi-nuclide bioimaging experiments

The practical implementation of the strategy proposed in this work is demonstrated here in a bioimaging application on liver tissue sections. The results from the single-m/q runs indicated that the FW0.01M of all targeted elements is $\lesssim 50\ ms$; a pixel acquisition rate of 20 Hz was hence adopted. The SNRs were calculated based on a single scan in close proximity to the ablated region, using the variation of the single scan as an estimation of the standard deviation of the image noise. The SNR of the sample scan was ≈ 8, hence, a 5 µm spot size was deemed to be appropriate for mapping, keeping in mind the considerations made above. Two images on the same region were produced, one image with non-optimized and subsequently, another image using optimized data acquisition settings (Figure 6), following the guidelines set out in the previous sections. In Figure 6, (A) displays an image suffering from spectral skew and aliasing ($f/f_s = 0.96$), (B) has the sampling time synchronized to the repetition rate ($f/f_s = 2$). It is clearly evident from these images that aliasing can be highly detrimental to the image quality; the image affected by this artefact does not reflect the natural distribution of these (relatively homogenously distributed) elements. Thus, aliasing should be avoided at all costs.

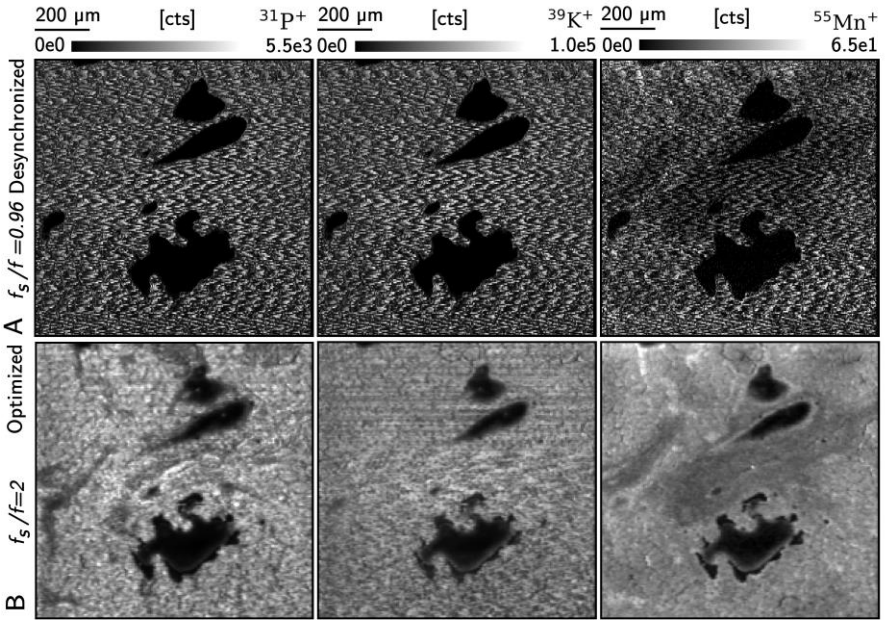

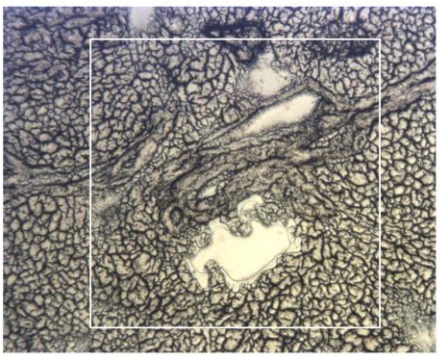

	A	B
Dwell time for ^{31}P [ms]	15	8.6
Dwell time for ^{39}K [ms]	15	5.5
Dwell time for ^{55}Mn [ms]	13.99	29.89
Sampling cycle [ms]	24.003	50.003

Figure 6 Elemental images from the bioimaging experiment. (A) The image produced on a region of the sample with the acquisition cycle not synchronized to the repetition rate ($f_s/f = 0.96$). (B) The image produced on the same region of the sample, using identical experimental parameters, but with the acquisition cycle timing synchronized to the repetition rate ($f_s/f = 2$). The right side of the figure shows a microscopy image of the ablated zone prior to ablation. In the table, the optimized set of acquisition settings in the bioimaging experiment are provided. The header of the table refers to the respective elemental images in this figure.

5. Conclusions

Temporal aliasing is an important issue for low-dispersion laser ablation setups using single-collector mass spectrometers. By matching the acquisition rate to 2-3 times the repetition rate, the integration windows are positioned such that a stable response can be captured for each nuclide and aliasing can be evaded, despite the underlying transient signal being unstable (showing separated peak profiles). It should be noted that, although the response for the different nuclides cannot be traced back to a single pulse, the approach outlined here offers similar advantages as approaches where signal peaks are isolated and individually integrated, whilst providing higher sensitivity. From the peak profile width, the optimum acquisition rate, repetition rate, and scan speeds can be derived. Furthermore, a single sample scan permits to tailor the distribution of the available dwell time for each nuclide of interest as to achieve a higher image contrast. The Rose Criterion forms a guideline to the most appropriate spot size here, after which the scan speeds can be recalculated.

6. Notes

The authors declare the following competing financial interest(s):

This work was partly funded by Teledyne CETAC Technologies.

7. Acknowledgements

The authors acknowledge Teledyne CETAC Technologies and the Flemish Research Foundation (FWO) for financial and/or logistic support. Stijn J. M. Van Malderen is a Ph.D. fellow of the FWO [grant number G017217N]. Frank Vanhaecke acknowledges BOF-UGent for funding under the form of a concerted research action (GOA) [grant number 2017000403].

8. References

[1] O. Borovinskaya, B. Hattendorf, M. Tanner, S. Gschwind, D. Günther, A prototype of a new inductively coupled plasma time-of-flight mass spectrometer providing temporally resolved, multi-element detection of short signals generated by single particles and droplets, J. Anal. At. Spectrom., 28 (2013) 226-233.

[2] T. Pettke, C.A. Heinrich, A.C. Ciocan, D. Gunther, Quadrupole mass spectrometry and optical emission spectroscopy: detection capabilities and representative sampling of short transient signals from laser-ablation, J Anal Atom Spectrom, 15 (2000) 1149-1155.

[3] M. Harlaux, O. Borovinskaya, D.A. Frick, D. Tabersky, S. Gschwind, A. Richard, D. Günther, J. Mercadier, Capabilities of sequential and quasi-simultaneous LA-ICPMS for the multi-element analysis of small quantity of liquids (pl to nl): insights from fluid inclusion analysis, J. Anal. At. Spectrom., 30 (2015) 1945-1969.

[4] S.J.M. Van Malderen, A.J. Managh, B.L. Sharp, F. Vanhaecke, Recent developments in the design of rapid response cells for laser ablation-inductively coupled plasma-mass spectrometry and their impact on bioimaging applications, J. Anal. At. Spectrom., 31 (2016) 423-439.

[5] A. Gundlach-Graham, D. Gunther, Toward faster and higher resolution LA-ICPMS imaging: on the co-evolution of LA cell design and ICPMS instrumentation, Analytical and bioanalytical chemistry, 408 (2016) 2687-2695.

[6] J.T. van Elteren, A. Izmer, M. Šala, E.F. Orsega, V.S. Šelih, S. Panighello, F. Vanhaecke, 3D laser ablation-ICP-mass spectrometry mapping for the study of surface layer phenomena – a case study for weathered glass, J Anal Atom Spectrom, 28 (2013) 994-1004.

[7] L. Feng, J. Wang, Evaluation of mixing devices and connection mode in the determination of Pb in glass using online isotope dilution laser ablation-ICP-MS, J. Anal. At. Spectrom., 29 (2014) 2183-2189.

[8] J. Pisonero, C. González-Gago, M. Iglesias, R. Cuervo, D. Blanco, H. Stoll, N. Bordel, Fast wash-out cells and aerosol mixing devices for geochemical applications of LA-ICP-MS, in: European Workshop on Laser ablation 2016, Ljubljana, Slovenia, 2016.

[9] S.E. Gilbert, L.V. Danyushevsky, T. Rodemann, N. Shimizu, A. Gurenko, S. Meffre, H. Thomas, R.R. Large, D. Death, Optimisation of laser parameters for the analysis of sulphur isotopes in sulphide minerals by laser ablation ICP-MS, J Anal Atom Spectrom, (2014).

[10] D. Bleiner, F. Belloni, D. Doria, A. Lorusso, V. Nassisi, Overcoming pulse mixing and signal tailing in laser ablation inductively coupled plasma mass spectrometry depth profiling, J Anal Atom Spectrom, 20 (2005) 1337-1343.

[11] C.C. Garcia, H. Lindner, K. Niemax, Laser ablation inductively coupled plasma mass spectrometry—current shortcomings, practical suggestions for improving performance, and experiments to guide future development, J Anal Atom Spectrom, 24 (2009) 14-26.

[12] J.T. van Elteren, F. Vanhaecke, Angular resolution dependency in 2D LA-ICP-MS mapping – the case for low-dispersion laser ablation cells, J. Anal. At. Spectrom., 31 (2016) 1998-2004.

[13] J.T. van Elteren, A. Izmer, V.S. Selih, F. Vanhaecke, Novel Image Metrics for Retrieval of the Lateral Resolution in Line Scan-Based 2D LA-ICPMS Imaging via an Experimental-Modeling Approach, Anal Chem, 88 (2016) 7413-7420.

[14] P.K. Diwakar, J.J. Gonzalez, S.S. Harilal, R.E. Russo, A. Hassanein, Ultrafast laser ablation ICP-MS: role of spot size, laser fluence, and repetition rate in signal intensity and elemental fractionation, J Anal Atom Spectrom, 29 (2014) 339-346.

[15] N.J.G. Pearce, W.T. Perkins, J.A. Westgate, M.P. Gorton, S.E. Jackson, C.R. Neal, S.P. Chenery, A compilation of new and published major and trace element data for NIST SRM 610 and NIST SRM 612 glass reference materials, Geostandard Newslett, 21 (1997) 115-144.

[16] R.F.J. Dams, J. Goossens, L. Moens, SPECTRAL AND NON-SPECTRAL INTERFERENCES IN INDUCTIVELY-COUPLED PLASMA MASS-SPECTROMETRY, Mikrochim Acta, 119 (1995) 277-286.

[17] E.H. Evans, J.J. Giglio, Interferences in inductively coupled plasma mass spectrometry. A review, J Anal Atom Spectrom, 8 (1993) 1-18.

[18] A.J.R. Kent, Lead isotope homogeneity of NIST SRM 610 and 612 glass reference materials: Constraints from laser ablation multicollector ICP-MS (LA-MC-ICP-MS) analysis, Geostandards and Geoanalytical Research, 32 (2008) 129-147.

[19] R.W. Hinton, B. Harte, G. Witteickschen, Ion Probe Measurements of National-Institute-of-Standards-and-Technology Standard Reference Material Srm-610 Glass, Trace-Elements, Analyst, 120 (1995) 1315-1319.

[20] Teledyne CETAC Technologies Inc., Aerosol Rapid Introduction System, in.

[21] W. Müller, M. Shelley, P. Miller, S. Broude, Initial performance metrics of a new custom-designed ArF excimer LA-ICPMS system coupled to a two-volume laser-ablation cell, J Anal Atom Spectrom, 24 (2009) 209.

[22] D. Gunther, I. Horn, B. Hattendorf, Recent trends and developments in laser ablation-ICP-mass spectrometry, Fresenius J. Anal. Chem., 368 (2000) 4-14.

[23] H.A. Wang, D. Grolimund, C. Giesen, C.N. Borca, J.R. Shaw-Stewart, B. Bodenmiller, D. Gunther, Fast chemical imaging at high spatial resolution by laser ablation inductively coupled plasma mass spectrometry, Anal Chem, 85 (2013) 10107-10116.

[24] A.M. Leach, G.M. Hieftje, Factors affecting the production of fast transient signals in single shot laser ablation inductively coupled plasma mass spectrometry, Applied Spectroscopy, 56 (2002) 62-69.

[25] A. Gutiérrez-González, C. González-Gago, J. Pisonero, N. Tibbetts, A. Menéndez, M. Vélez, N. Bordel, Capabilities and limitations of LA-ICP-MS for depth resolved analysis of CdTe photovoltaic devices, J. Anal. At. Spectrom., 30 (2015) 191-197.

[26] D. Bleiner, A. Bogaerts, Computer simulations of laser ablation sample introduction for plasma-source elemental microanalysis J Anal Atom Spectrom, 21 (2006) 1161-1174.

[27] M. Costas-Rodríguez, T. Van Acker, A.A.M.B. Hastuti, L. Devisscher, S. Van Campenhout, H. Van Vlierberghe, F. Vanhaecke, Laser ablation-inductively coupled plasma-mass spectrometry for quantitative mapping of the copper distribution in liver tissue sections from mice with liver disease induced by common bile duct ligation, J. Anal. At. Spectrom., (2017).

[28] I.A.E. Agency, Diagnostic Radiology Physics: A Handbook for Teachers and Students, International Atomic Energy Agency, 2014.

[29] A.E. Burgess, The Rose model, revisited, J Opt Soc Am A Opt Image Sci Vis, 16 (1999) 633-646.